Cooling Architecture Selection for Air-Cooled Data Centers by Minimizing Exergy Destruction

Rohit Gupta,[1,2] *Sahar Asgari,*[1,2] *Hosein Moazamigoodarzi,*[1,2] *Souvik Pal,*[1] *and Ishwar K. Puri* [1,2*]

[1]Computing Infrastructure Research Centre, McMaster University, Hamilton, Ontario, Canada

[2]Department of Mechanical Engineering, McMaster University, Hamilton, Ontario, Canada

Note: This is a preprint version of the published manuscript. The publisher full-text is available at doi.org/10.1016/j.energy.2020.117625

AUTHOR INFORMATION

***Corresponding author**

McMaster University

1280 Main St. W.

Hamilton, ON L8S 4L7, Canada

Email: ikpuri@mcmaster.ca

Abstract

Air-cooled Data Centers (DCs) require effective thermal management of the servers. This can be accomplished by implementing new cooling architectures. Nearly 33% of overall energy consumption is attributed to the cooling infrastructure, which indicates the importance of the specific cooling configuration. Our objective is to compare four emerging and traditional DC cooling architectures, (a) in-row cooling, (b) rack-mountable cooling (RMC), (c) underfloor air delivery (UFAD), and (d) overhead air delivery. Since a first law-based energy analysis of a DC cooling architecture seldom considers irreversibility and component level inefficiency, an exergy-based analysis provides an alternate basis for assessment. We propose a methodology that combines Computational Fluid Dynamics simulations with thermodynamic energy and exergy balances to determine the exergy loss in different components in DC. A dimensionless parameter is identified to characterize the exergy loss as a function of the Peclet number and the dimensionless dead state temperature ratio. The architecture containing RMC units has the lowest exergy loss. The chiller loss constitutes up to 55% of the overall exergy loss. This analysis facilitates better decision making and design choices for air-cooled DCs on the basis of minimization of thermodynamic irreversibility with the purpose of lowering energy waste.

Key words:
Data Center; Exergy destruction; Distributed Cooling; Energy efficiency; Irreversibility.

Nomenclature:

Uppercase

C_{pa}	Specific heat capacity of air (J kg^{-1} K^{-1})
C_{pw}	Specific heat capacity of water (J kg^{-1} K^{-1})
L_c	Characteristic length scale (m)
N	Number of servers in the data center
$\dot{Q}_s$	Power consumption of each server (W)
R_s	Server thermal resistance (K W^{-1})
$\dot{S}'''_{HT}$	Heat transfer entropy generation per unit volume (W m^{-3} K^{-1})
$\dot{S}'''_{VD}$	Viscous dissipation entropy generation per unit volume (W m^{-3} K^{-1})
$\bar{T}$	Mean temperature in each control volume
T_{ca}	Cold air supply temperature (K)
T_{cw}	Chilled water supply temperature (K)
T_{ha}	Mean hot air return temperature (K)
T_{hw}	Return water temperature (K)
$T_{ha,0}$	Exhaust air temperature rejected by chiller condenser to ambient (K)
T_i	Server inlet temperature (K)
T_o	Server exhaust temperature (K)
T_s	Server mean boundary temperature (K)
T_0	Ambient dead state temperature (K)
U_c	Characteristic velocity scale (m s^{-1})
$\dot{W}$	Power consumption of chiller (W)

Lowercase

g	Gravitational acceleration (m s^{-2})
k	Specific turbulent kinetic energy (m^2 s^{-2})
$\dot{m}_s$	Mass flowrate of air through server (kg s^{-1})
$\dot{m}_w$	Mass flow rate of water (kg s^{-1})
$\bar{u}$	Mean velocity component in x-direction (m s^{-1})
$\bar{v}$	Mean velocity component in y-direction (m s^{-1})
$\bar{w}$	Mean velocity component in z-direction (m s^{-1})
x	Horizontal co-ordinate (m)
y	Vertical co-ordinate (m)
z	Depth co-ordinate (m)

Greek Letters

α	Thermal diffusivity of air (m^2 s^{-1})
β	Co-efficient of thermal expansion (K^{-1})
ε	Turbulent kinetic energy dissipation rate (m^2 s^{-3})
ζ	Dimensionless dead state temperature ratio $[T_0/(T_{ha} - T_{ca})]$
η	Dimensionless exergy loss $[\dot{\psi}_{d,t}/\dot{Q}_{IT}]$
λ	Thermal conductivity (W m^{-1} K^{-1})
μ	Dynamic viscosity (kg m^{-1} s^{-1})
ρ	Density (kg m^{-3})
$\dot{\psi}_{d,a}$	Total airspace exergy loss component (W)
$\dot{\psi}_{d,c}$	Chiller exergy loss component (W)
$\dot{\psi}_{d,h}$	Heat exchanger exergy loss component (W)
$\dot{\psi}_{d,s}$	Total exergy loss components in servers (W)
$\dot{\psi}'''_{HT}$	Exergy destruction due to heat transfer in each control volume of airspace (W m^{-3})
$\dot{\psi}'''_{VD}$	Exergy destruction due to viscous dissipation in each control volume of airspace (W m^{-3})

p	Pressure (N m^{-2})	***Miscellaneous***	
$\dot{m}_a$	Mass flowrate of air through cooling unit (kg s^{-1})	Pr_t	Turbulent Prandtl number
$\dot{m}_f$	Total mass flowrate of air through chiller condenser fans (kg s^{-1})	Pe	Peclet number

1. Introduction

Data Centers (DC) are meticulously designed facilities that house complex IT equipment (ITE), which includes servers, network switches, routers, storage systems, and network firewalls. Due to the essential services that they enable, e.g., banking, healthcare, and defense, DCs are often referred to as mission-critical facilities [1]. With hardware and software advances, the computational power of ITE is rapidly increasing, necessitating improvements in the cooling provided to it during runtime. Almost one-third of the total power consumption in a DC is associated with cooling, which provides an opportunity to identify potential areas for savings [2, 3]. Although liquid-cooled DCs are much more energy-efficient [4, 5], they require a complex plumbing loop. Hence, most DCs are designed to house air-breathing servers. These servers draw in cold air for cooling and exhaust the heated air. The turbulent airflow in a DC is a dynamically changing vector field. Consequently, the choice of cooling architecture has a significant influence on the system energy efficiency [6, 7].

Broadly, four cooling architectures are employed, (1) underfloor air delivery (UFAD), (2) overhead air delivery (OHAD), (3) in-row cooling (IRC), and (4) rack-mountable cooling units (RMCU). The first two systems are more common, while the latter two are relatively new. There are two primary air distribution inefficiencies in a DC, hot air recirculation and cold air bypass [8]. A poorly managed DC airspace has a cascading detrimental effect on other cooling components, such as the computer room air handler (CRAH) unit, chillers, and cooling towers, increasing overall cooling energy consumption in a DC for a specific IT load.

The literature provides energy assessments of DC cooling architectures based on the first law of thermodynamics [6, 7], and uses temperature-based metrics, such as supply heat index *SHI*, return heat index *RHI*, rack temperature index *RTI*, rack cooling index *RCI*, negative pressure ratio

NP, recirculation ratio *R*, bypass ratio *BP*, and balance ratio *BAL* to characterize airspace inefficiencies [9-11]. Analyses based on the first law of thermodynamics only account for the amount of energy spent and not the irreversibility due to entropy generation. Since they cannot quantify the waste of available energy, these first law methods are insufficient for developing designs for effective thermal management of air-cooled DCs. To better understand cooling inefficiencies, an analysis based on the second law of thermodynamics that characterizes exergy destruction in a DC becomes essential.

The transport of heat in an air-cooled DC occurs across multiple components, e.g., the CPU, copper heat sink on the CPU, airflow through the heat sink, air to liquid heat exchanger, and heat transfer from the liquid to refrigerant and refrigerant to ambient air. Since exergy destruction during these stages is associated with the additional power consumed for cooling, it becomes possible to identify system design features that lead to cooling inefficiencies.

The literature on exergy-based assessments that can guide improvements in DC design is sparse. It includes full system modeling of the exergy loss in a DC for a conventional UFAD configuration using a thermodynamic energy and exergy balance methodology known as the indirect method [12-17]. These investigations identify how exergy destruction occurs in each DC component due to varying rack operation conditions, IT load density, cooling unit operating parameters, and chiller and cooling tower operation. The direct method to determine exergy destruction requires fluid dynamics solutions. Here, computational fluid dynamics (CFD) based solutions of Reynolds averaged Navier Stokes (RANS) equations can be used to resolve the flow inside a DC airspace, e.g., to determine the exergy loss in the UFAD and OHAD architectures that are popular in legacy DCs [18-20]. The former type of architecture is an underfloor perforated tile-based cooling system, whereas the latter type employs an overhead cooling system. For these

architectures, since the volume of air handled is prodigious and occurs over large flow path lengths, the corresponding pressure drops introduce inefficiencies in the system. Both architectures are also prone to hot air recirculation and cold air bypass.

Although legacy architectures employ room-based cooling architectures, the RMCU is promising for high-density computing infrastructure [21-23]. Such a scheme consists of a rack-mountable cooling system placed inside each rack that has separated hot and cold chambers. A version of the RMCU suitable for a high density scalable modular DC is the IRC that simultaneously delivers cooling air to several racks to reduce hot-spots [24, 25]. The IRC architecture is an enclosed row-based cooling solution that provides cold air to several IT racks stacked beside one another. Placing the cooling units nearer to the heat sources, i.e., the servers reduces the airflow path length, which in turn reduces the adverse effects due to pressure drops. Doing so also reduces hot and cold air mixing. An exergy-based assessment of the improvement in energy consumption by a modular (i.e., RMCU and IRC) DC as compared to a legacy DC is yet unavailable. Hence, there is a lack of guidance for DC designers for selecting a suitable cooling architecture. This leads to cooling overdesign, often by a factor greater than two, producing energy waste and considerably increasing the total cost of ownership (TCO).

We develop a methodology that compares different cooling architectures based on their contributions to exergy destruction. The airspace exergy loss parameters are obtained with a direct method, whereas an indirect method was applied to quantify exergy losses in servers, CRAH units, and the chiller. This hybrid approach provides full system exergy modeling, i.e., extending from servers to chillers while reducing computational expense. The method is used to compare four different cooling schemes (UFAD, OHAD, IRC, and RMCU). For each geometry, seven different scenarios are considered by varying the operation of the DC cooling unit, and the resulting impact

on component level exergy loss is identified. Finally, a dimensionless parameter to characterize overall exergy destruction in DC is identified.

The novelty of the study lies in the development of a hybrid method that characterizes exergy destruction in a DC and thus comparing different cooling architectures. A dimensionless parameter is a facile tool that provides designers with guidance on how to minimize overall exergy loss in a DC. The method identifies (a) designs for optimal cooling, (b) component level inefficiencies, (c) favorable air delivery schemes, (d) the impact of operating conditions on cooling energy wastage, and (e) it also minimizes exergy destruction.

Our objectives are to (1) demonstrate that the exergy destruction minimization approach is suitable for comparing the performance of DC cooling systems, (2) investigate the component level irreversibility in servers, DC airspace, CRAH unit, and chillers, (3) compare different cooling architectures for which we have selected the UFAD, OHAD, IRC, and RMCU configurations, (4) investigate the influence of cooling unit airflow on the exergy destruction that occurs in different DC components, (5) propose strategies to minimize exergy loss in each component, and (6) identify a dimensionless parameter that characterizes the overall exergy loss in a DC.

2. Methodology

We consider a 63 kW air-cooled DC that uses CRAH units, and air-cooled chillers to reject the heat from the DC airspace. Figure 1 presents the thermal interactions across the DC components. Servers generate heat that is removed by cold air supply, and the warmer server exhaust is returned to the CRAH units, which employ air to water heat exchanger to remove heat from the airside and transfer it to the waterside. A pump-driven chilled water circulation loop connects the waterside of the CRAH units to an air-cooled chiller that rejects heat to the ambient. The chiller has a nominal

design capacity of 88 kW [26]. While other options for the chiller are available for DCs with higher capacities, such as a water-cooled chiller that rejects heat to the cooling tower [17], our selection is nevertheless representative for comparing component level losses (e.g., in servers, airspace, CRAH, pumps, and chillers) and the overall exergy destruction due to changes in the cooling architecture.

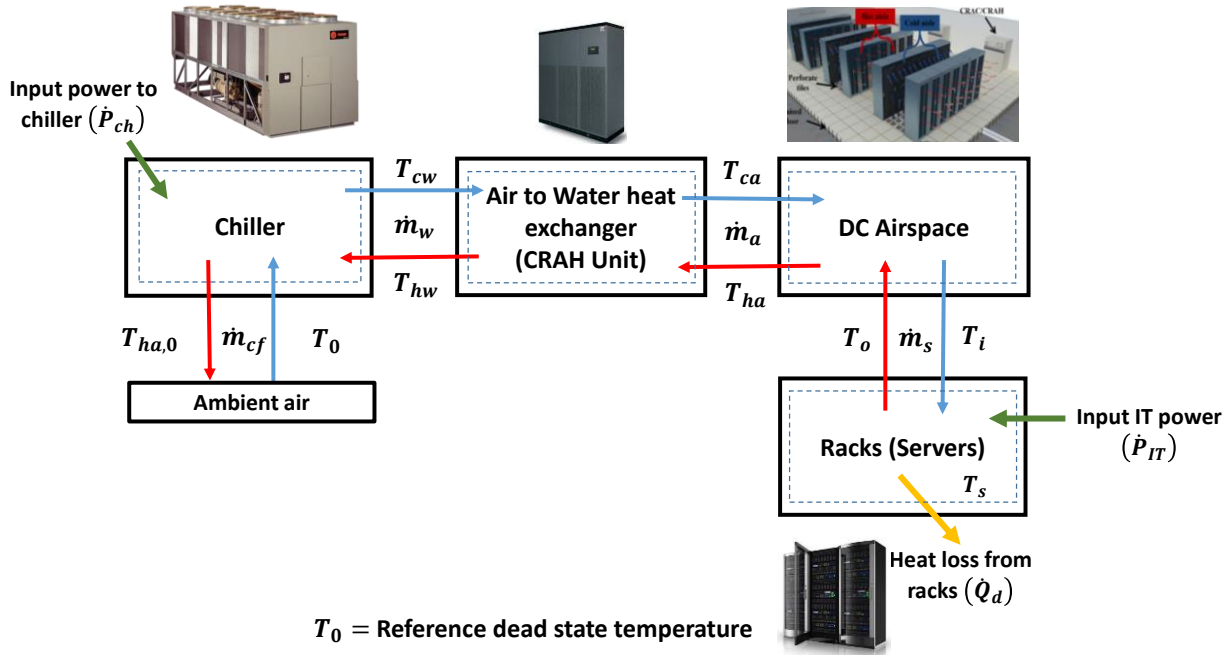

Figure 1: Thermal interactions during heat removal from the rack to the ambient.

In an air-cooled DC, exergy destruction depends on the (1) the cooling architecture, (2) flowrate of cold air delivery, and (3) the mismatch between server suction temperature and cooling unit set-point. By decomposing the overall exergy destruction for its principal components, we obtain the exergy destruction in the (1) servers, (2) heat exchanger inside the CRAH unit, (3) fans inside the CRAH unit, (4) DC airspace, (5) chilled water pumps, and (6) chillers. Items 3 and 5 consume 4% and 7% of the total cooling power, respectively. The efficiencies of the pumps and fans used in DC are assumed to be 75% [7, 17, 27], i.e., exergy destruction in pumps and fans is negligible (of the order of 2 to 3 %) compared to the magnitude of overall exergy loss. Therefore,

we only determine the exergy loss components associated with the (a) servers, (b) airspace, (c) heat exchanger inside CRAH units, and (d) chillers for different cooling schemes.

To determine the exergy destruction for these components, the following conditions must be determined or assumed, (1) thermodynamic dead state temperature (assumed at a constant value of 295.15 K), (2) total IT load, which is 63 kW in our case, (3) airspace field variables, i.e., pressure, temperature, velocities, and turbulence parameters, (4) CRAH airflow, (5) CRAH set-point, (6) airside return temperature to CRAH units, (7) supply chilled water temperature to CRAH, (8) return water temperature from CRAH, (9) chilled water flow rate, (10) ambient air temperature supplied to the chiller (assumed to equal to the thermodynamic dead state temperature), (11) heat rejection temperature to the ambient from chiller, and (12) airflows of chiller fans.

To compare operation over a range of operating parameters for different cooling architectures, the airflow through the CRAH unit is varied, as shown in Table 1. Following the appropriate ASHRAE guideline for safe operation of servers, the maximum server intake temperatures are held below 26.5 °C [28, 29] for all the scenarios simulated. Since the cooling unit supply temperature is specified, the resulting airflow and return temperatures are determined using CFD for different air delivery schemes. The airside and waterside parameters are coupled by using the $\varepsilon - NTU$ method [6, 17, 30] for heat exchangers within the CRAH units for different cooling architectures.

Table 1: Parametric and geometric variation

IT load (kW)	Geometry	Cold air supply temperature (°C)	Total volume flow rate of air ($m^3 s^{-1}$)	Maximum temperature in the cold aisle (°C)
63	UFAD	18	2.53	26.5
	OHAD		3.04	
			3.54	
	IRC		4.05	
			4.56	
	RMCU		5.06	
			5.57	

2.1. Geometries and physical considerations for CFD simulation

The turbulent flow field in the DC airspace is resolved through CFD simulations using ANSYS Fluent 18.0 software. The RANS equations are coupled with the energy equation and a standard $k - \varepsilon$ model [6, 18-20, 31-33] for steady-state, incompressible flow, and a Boussinesq approximated body force to determine the velocity, temperature and turbulence fields. Figure 2 provides a schematic representation of the different air delivery schemes considered, which are (a) UFAD, (b) OHAD, (c) IRC, and (d) RMCU. For all architectures, we consider 6 IT racks of standard dimensions ($2 \times 1 \times 0.6\ m^3$), each consisting of 40 1U (Model: HP ProLiant DL360 G5) servers. Each rack has an IT load of 10.5 kW distributed over 40 servers and an airflow of $0.57\ m^3\ s^{-1}$, where each server has an airflow of $0.01415\ m^3\ s^{-1}$ [21].

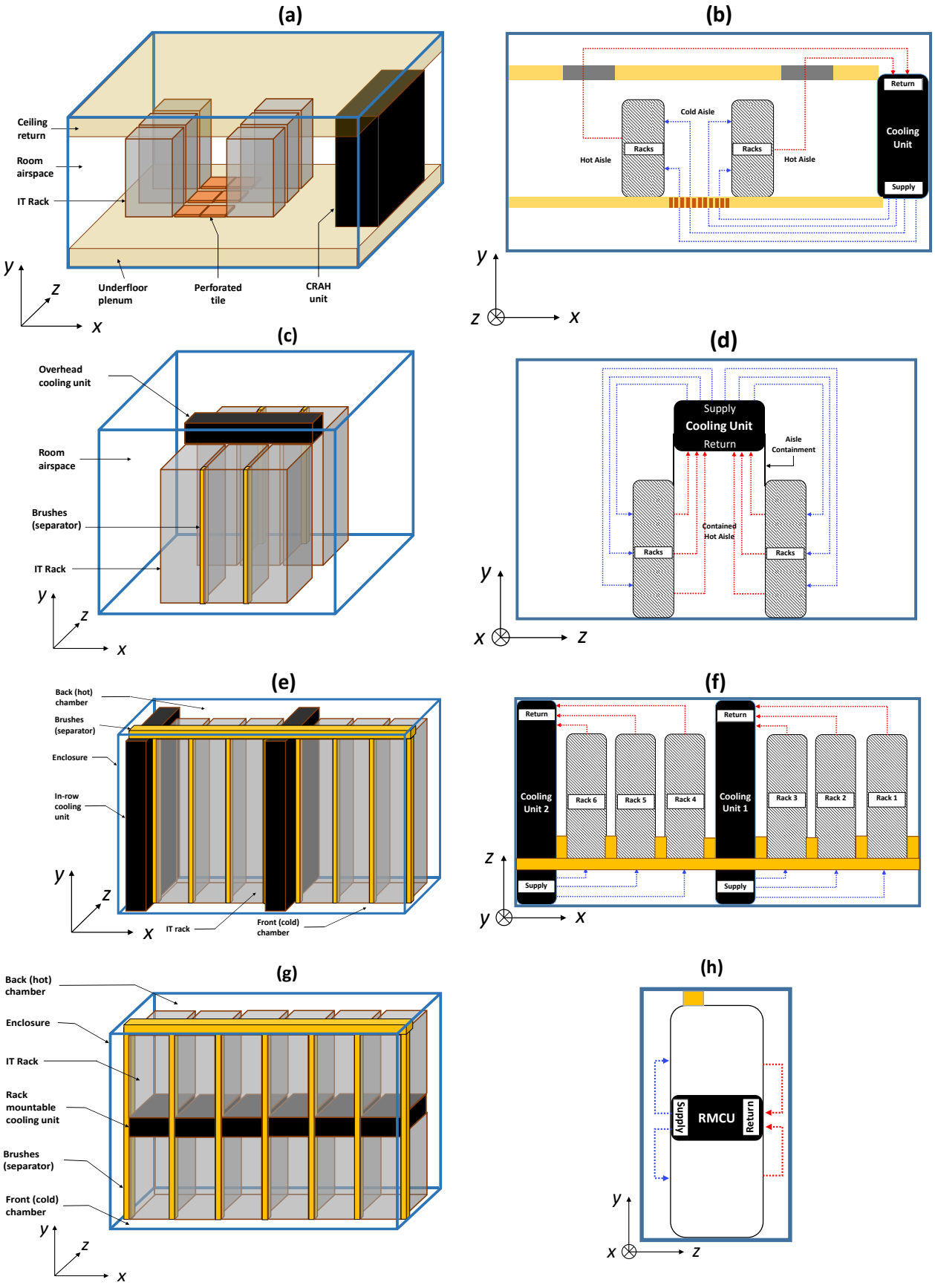
(a)
Ceiling return
Room airspace
IT Rack
Underfloor plenum
Perforated tile
CRAH unit
y
z
x
(b)
Return
Cooling Unit
Supply
Cold Aisle
Racks
Racks
Hot Aisle
Hot Aisle
y
z
x
(c)
Overhead cooling unit
Room airspace
Brushes (separator)
IT Rack
y
z
x
(d)
Supply
Cooling Unit
Return
Aisle Containment
Contained Hot Aisle
Racks
Racks
y
x
z
(e)
Back (hot) chamber
Brushes (separator)
Enclosure
In-row cooling unit
IT rack
Front (cold) chamber
y
z
x
(f)
Return
Return
Cooling Unit 2
Rack 6
Rack 5
Rack 4
Cooling Unit 1
Rack 3
Rack 2
Rack 1
Supply
Supply
z
y
x
(g)
Back (hot) chamber
Enclosure
IT Rack
Rack mountable cooling unit
Brushes (separator)
Front (cold) chamber
y
z
x
(h)
Supply
RMCU
Return
y
x
z

Figure 2: Schematic representation of the geometries used to simulate four cooling architectures: (a)-(b) UFAD, (c)-(d) OHAD, (e)-(f) IRC, (g)-(h) RMCU. Blue and red dotted lines depict cold and hot airflows through the racks respectively.

Based on the sizes of the CRAH units available for the different configurations, e.g., the internal heat exchanger size, number, and capacity of fans, a cooling architecture requires a specific number of cooling units to handle the heat load of Table 1. For UFAD cooling (Figure 2a and 2b), a room-based cooling system is used that consists of a CRAH unit, underfloor plenum, perforated tiles and a ceiling return to the CRAH. Cold air from the CRAH unit passing through the underfloor plenum is delivered into the cold aisle through perforated tiles. The perforated tiles are modeled through an additional momentum source using the modified body force (MBF) model [32, 33]. Racks are arranged in two rows, where each row consists of 3 racks. The server intakes are placed in the cold aisle, and hot air from the exhaust is guided to the ceiling return using two overhead ducts.

For OHAD cooling (Figure 2c and 2d), we consider a contained hot aisle [19, 20] and three overhead CRAH units, where each unit handles two racks. The cold air is delivered to the room from the overhead CRAH unit, whereupon it passes through the server, is exhausted into the hot aisle, and then drawn back into the CRAH unit.

For IRC cooling (Figure 2e and 2f), two CRAH units are employed, where each unit handles 3 IT racks. All the 6 racks and 2 cooling units are arranged in a single row within a container, as shown in Figure 2e. Cold air delivered by in-row cooling units passes through the servers and is released into the hot aisle (or back chamber).

The RMCU cooling scheme utilizes a rack-mountable CRAH unit of 2U size for each rack, resulting in 6 CRAH units for our case. These cooling units are placed at the midway height of the rack and deliver cold air vertically (Figure 2g and 2h).

The IT racks are represented by the recirculation boundary condition available in ANSYS Fluent that uses a thermodynamic energy balance to determine the rack exhaust temperature for a specified heat load and flowrates through servers. The flowrate and power consumption for the servers are known for a specific DC utilization. The CRAH unit inlet and exhaust zones are emulated using the inlet mass flow at a certain temperature (which is the cooling unit set-point) and outlet pressure for a target mass flow rate, respectively. Table 2 shows the specifications of cooling units used for different architectures.

A steady-state assumption is imposed, which results in temporally invariant airflow through the racks and cooling units, the heat loads through the servers, and the air delivery temperature from the cooling units. In commercial DCs the gaps between the racks or those between a rack and its containment walls produce mixing of the hot and cold airstreams, but this is usually minimized by inserting high-density air blocking brushes at these locations [6, 31]. The brushes provide flow resistance and minimize momentum and energy transport across aisles. To represent the effect of brushes in the CFD simulation, they are modeled as porous media using a power-law resistance so that [6],

$$\Delta p = -C_0 |v|^{C_1}, \tag{1}$$

where, $C_0 = 11$ and $C_1 = 1.15$ are determined from experiments.

Table 2: Geometric considerations for CFD simulation

Architecture	Maximum cooling capacity of each unit (kW)	Size of each cooling unit (m^3)	Maximum volume flow rate of air ($m^3\ s^{-1}$) through each unit	Number of cooling units used for present study
IRC	33	1.2 × 0.3 × 2.0	2.01	2
UFAD	66	1.2 × 2.4 × 3.0	4.02	1
RMCU	11	0.6 × 0.1 × 1.0	0.67	6
OHAD	22	0.6 × 0.3 × 1.2	1.34	3

2.2. Exergy loss: Server/Rack component

The electrical power consumption of each server is assumed to be fully converted into heat, $\dot{Q}_s$, resulting in a server exhaust temperature,

$$T_o = T_i + \frac{\dot{Q}_s}{\dot{m}_s C_{pa}}, \tag{2}$$

where T_i denotes the inlet temperature to the server, and $\dot{m}_s$ the air mass flowrate through servers. For each server, the effective surface temperature T_s is calculated using a lumped thermal resistance approximation [17, 34],

$$T_s = T_i + \frac{\dot{Q}_s}{\dot{m}_s C_{pa}\left[e^{-\frac{1}{\dot{m}_s C_{pa} R_s}} - 1\right]}, \tag{3}$$

where R_s denotes the thermal resistance for the 1U server, which is 0.065 K/W [17]. With T_s, T_i and T_o known, the total exergy destruction with *N* servers $\dot{\psi}_{d,s}$ (see Figure 1),

$$\dot{\psi}_{d,s} = N\left\{\dot{m}_s C_{pa}\left[\left(T_i - T_o\right) - T_0 \ln\left(\frac{T_i}{T_o}\right)\right] + \dot{Q}_s\left[1 - \frac{T_0}{T_s}\right]\right\}. \tag{4}$$

We consider a DC with 6 racks, each rack having 40 1U servers with identical exergy destruction. Since the rack load is constant, the exergy destruction attributed to the server is also constant. The salient characteristics of the servers and IT racks are listed in Table 3.

Table 3: Server and IT rack parameter specifications.

Parameter	Value
Model	HP ProLiant DL360 G5
Server chassis size	1U
Power Consumption	262.5 W
Airflow rate	0.01415 m^3 s^{-1}
Thermal resistance	0.65 K W^{-1}
Number of servers	40
Rack type	Standard 42U racks (1U = 1.75 inch)
Number of racks	6

2.3. Exergy loss: Airspace component

The exergy destruction associated with the airspace helps identify inefficiencies, cooling air maldistribution, and mismanagement of cooling architectures. This term is important for assessing the impact of different geometries, airflow management strategies, and cooling unit operating conditions on the exergy loss.

The airflow velocity, pressure, temperature, and turbulence in each control volume are determined through CFD simulations for different cooling architectures and operating parameters, as described in Table 2. The exergy destruction formulation for turbulent flows utilizing the $k-\varepsilon$ model is as follows [18, 35-38].

Entropy generation:

$$\dot{S}'''_{VD} = \frac{\mu}{\overline{T}}\left\{2\left[\left(\frac{\partial \overline{u}}{\partial x}\right)^2+\left(\frac{\partial \overline{v}}{\partial y}\right)^2+\left(\frac{\partial \overline{w}}{\partial z}\right)^2\right]+\left(\frac{\partial \overline{u}}{\partial y}+\frac{\partial \overline{v}}{\partial x}\right)^2+\left(\frac{\partial \overline{u}}{\partial z}+\frac{\partial \overline{w}}{\partial x}\right)^2+\left(\frac{\partial \overline{v}}{\partial z}+\frac{\partial \overline{w}}{\partial y}\right)^2\right\}+\frac{\rho\varepsilon}{\overline{T}} \quad (5)$$

$$\dot{S}'''_{HT} = \frac{\lambda}{\overline{T}^2}\left(1+\frac{C_\mu}{\alpha \,\mathrm{Pr}_t}\frac{k^2}{\varepsilon}\right)\left[\left(\frac{\partial \overline{T}}{\partial x}\right)^2+\left(\frac{\partial \overline{T}}{\partial y}\right)^2+\left(\frac{\partial \overline{T}}{\partial z}\right)^2\right]. \quad (6)$$

Exergy destruction:

$$\dot{\psi}'''_{HT} = T_0 \dot{S}'''_{HT}, \quad (7)$$

$$\dot{\psi}'''_{VD} = T_0 \dot{S}'''_{VD}, \quad (8)$$

$$\dot{\psi}'''_{d} = \dot{\psi}'''_{HT} + \dot{\psi}'''_{VD}, \text{ and} \quad (9)$$

$$\dot{\psi}_{d,a} = \iiint_V \dot{\psi}'''_d dxdydz. \quad (10)$$

Airspace exergy loss in a DC consists of two components, (a) exergy destruction due to unwanted heat transfer between the cold and hot air streams, and (b) exergy destruction due to pressure drop or turbulent velocity fluctuations. The heat transfer is determined using Eq. 6, and

the velocity gradient component is determined using Eq. 5. Once the CFD solution converges, Eqs. (5) – (9) are solved using a user-defined function (UDF) code in ANSYS Fluent 18.0 to obtain the exergy destruction inside each control volume. Subsequently, the volume integral of exergy destruction is determined using Eq. 10, which represents the loss of available energy.

2.4. Exergy loss: CRAH unit component

The air-water heat exchanger within the CRAH unit is the major exergy loss component. For the heat exchanger, the velocity gradient and turbulent exergy loss components have been shown to be insignificant [17, 18, 39]. Additional assumptions include (a) no boundary heat transfer between the system and its surroundings, and (b) negligible kinetic and potential energy changes. Thus, the exergy loss within the CRAH unit can be represented through the exergy balance across control volume (see Figure 1),

$$\dot{\psi}_a = \dot{m}_a C_{pa}\left[\left(T_{ha} - T_{ca}\right) - T_0 \ln\left(\frac{T_{ha}}{T_{ca}}\right)\right], \tag{11}$$

$$\dot{\psi}_w = \dot{m}_w C_{pw}\left[\left(T_{cw} - T_{hw}\right) - T_0 \ln\left(\frac{T_{cw}}{T_{hw}}\right)\right], \text{ and} \tag{12}$$

$$\dot{\psi}_{d,h} = \dot{\psi}_a + \dot{\psi}_w, \tag{13}$$

where $\dot{\psi}_a$ denotes the exergy lost by the airside and $\dot{\psi}_w$ that gained by the waterside.

From Eqs. (11) – (13), we note that the exergy loss associated with the heat exchanger is a function of the air mass flowrate $\dot{m}_a$, return temperature of air to CRAH T_{ha}, supply air temperature from CRAH T_{ca}, mass flowrate of water $\dot{m}_w$, inlet water temperature to CRAH T_{cw}, and outlet water temperature from CRAH T_{hw}. For a prescribed airflow and supply temperature from the CRAH, the return temperature to the CRAH unit is determined from the CFD simulations using the UDF in Fluent.

The airside parameters available from CFD simulation are coupled with the waterside parameters using a code is written in MATLAB™ 2015 that models the heat exchangers within the CRAH. The code employs the $\varepsilon - NTU$ method [6, 17, 30] for coupling the waterside and airside parameters by specifying the type and size of the heat exchanger inside the CRAH. The dimensions and types of heat exchangers selected for the IRC, UFAD, RMCU, and OHAD cooling configurations are shown in Table 4. The water flowrates for different heat exchangers are based on commercially available CRAH units.

Table 4: Heat exchanger characteristics [19, 40, 41].

Architecture	Heat exchanger type	Heat exchanger size (m^3)	Maximum volume flow rate of water ($m^3\ s^{-1}$)	Number of heat exchangers used for present study
IRC	Fin-tube	0.20 × 0.70 × 2.00	0.0009	2
UFAD	Fin-tube	0.20 × 1.50 × 2.25	0.0050	1
RMCU	Plate-fin	0.30 × 0.35 × 0.12	0.0004	6
OHAD	Fin-tube	0.30 × 1.20 × 0.60	0.0007	3

2.5. Exergy loss: Chiller component

We consider an 88 kW chiller [26], which consists of a vapor compression refrigeration cycle and an ambient air-cooled condenser that supplies the required chilled water to the CRAH unit. Considering the chiller boundary as the control volume for energy interactions with the surroundings, the energy balance requires the electrical energy input into the chiller, energy transport through the chilled waterside, and energy interactions in the ambient airside. The chiller is assumed to be insulated. Thus the boundary heat transfer component is absent.

For the abovementioned conditions, the exergy destruction for the chiller (see Figure 1),

$$\dot{\psi}_{d,c} = \dot{W} + \dot{m}_w C_{pw}\left[\left(T_{hw} - T_{cw}\right) - T_0 \ln\left(\frac{T_{hw}}{T_{cw}}\right)\right] + \dot{m}_f C_{pa}\left[\left(T_0 - T_{ha,0}\right) - T_0 \ln\left(\frac{T_0}{T_{ha,0}}\right)\right]. \quad (14)$$

Imposing an energy balance across the chiller boundary control volume,

$$\dot{m}_w C_{pw}(T_{hw} - T_{cw}) + \dot{m}_f C_{pa}(T_0 - T_{ha,0}) + \dot{W} = 0. \quad (15)$$

Combining Eqs. (14) and (15), the chiller exergy loss,

$$\dot{\psi}_{d,c} = \dot{m}_w C_{pw} T_0 \ln\left(\frac{T_{cw}}{T_{hw}}\right) + \dot{m}_f C_{pa} T_0 \ln\left(\frac{T_{ha,0}}{T_0}\right). \quad (16)$$

To determine the exergy destruction associated with the chiller, the waterside, ambient airside, and the electric power consumption of the chiller must be determined. The total power consumption of the chiller is determined through the universal Ng-Gordon chiller model [42]. This model correlates the cooling load of the chiller evaporator, the air temperature entering the condenser, desired set-point of the chilled water leaving the evaporator, and the coefficient of performance (COP) as follows.

$$y = a_1 x_1 + a_2 x_2 + a_3 x_3, \quad (17)$$

$$x_1 = T_{cw}/Q_c, \quad (18)$$

$$x_2 = (T_0 - T_{cw})/(T_0 \times Q_c), \quad (19)$$

$$x_3 = [\{(1/COP) + 1\} \times Q_c]/T_0, \text{ and} \quad (20)$$

$$y = \{[(1/COP) + 1] \times (T_{cw}/T_0)\} - 1. \quad (21)$$

The coefficient of performance, COP, is the ratio of chiller evaporator heat load, Q_c, to the total electrical power consumption by the chiller $\dot{W}$, and T_{cw} denotes the chilled water temperature leaving the evaporator. Air entering the condenser is assumed to have a temperature equal to T_0. All temperatures are expressed in K and Q_c in kW. Data for Q_c, COP, T_{cw}, and T_0 are obtained from an 88kW chiller datasheet [26]. Fitting that data to Eqs. (17) – (21) using a multivariate regression solver, the chiller model is,

$$y = 0.026 x_1 + 28.872 x_2 + 0.241 x_3. \quad (22)$$

The waterside parameters (chilled water temperature supplied to CRAH, return water from CRAH, and water flowrate) are determined through the $\varepsilon - NTU$ method for the heat exchanger. Since the ambient air supply temperature is assumed equal to the thermodynamic dead state temperature (295.15 K), it is at zero exergy with respect to the ambient. The hot air temperature $T_{ha,0}$ returned to the ambient depends on the cooling load on the chiller and is determined from Eq. (15). The flow velocity of the chiller condenser fan $\dot{m}_f$ is obtained from the datasheet of the chiller [26]. The characteristics of the chiller are provided in Table 5.

Table 5: Chiller parameter and specifications.

Parameter	Value
Model	TRANE CGAF C25
Rated maximum capacity	25 ton of refrigeration (88 kW)
Airflow of condenser fans	10.22 $m^3\ s^{-1}$
Condenser air supply temperature	22 °C
Maximum chilled water flowrate	0.0019 $m^3\ s^{-1}$
Maximum chilled water flowrate	0.0057 $m^3\ s^{-1}$

3. Numerical procedure

The turbulent airflow field inside the DC is obtained by iteratively solving the RANS equations using the standard $k - \varepsilon$ model with ANSYS Fluent 18.0. The governing equations for mass, momentum, energy are solved for turbulence flow. Once convergence is obtained, the airspace exergy loss and the other components of exergy loss are calculated using thermodynamic energy-exergy balance equations. The simulation process is described in Appendix A1.

A mesh independence analysis provides the minimum number of nodes required for accurately representing the flow physics. Four meshes with 10^6, 1.7×10^6, 2.3×10^6, and 4×10^6 nodes provide different mesh geometries. The geometry with 2.3×10^6 nodes is selected for all cases due to its faster computation time while adequately determining the flow field. The RMS error for 60 different monitored nodes in the domain is lower than 1.5 ºC for this grid [43]. Table

6 provides mesh independence results for the average rack inlet temperature, hot air return temperature to the cooling unit, and volume integral of the airspace exergy loss. These are the primary quantities of interest determined from the CFD simulations.

Table 6: Mesh independence results.

Number of cells	Average rack inlet temperature (K)	Return temperature of air to cooling unit (K)	Volume integral of airspace exergy loss (W)
1.0×10^6	295.2	310.7	480.3
1.7×10^6	295.9	311.3	495.7
2.3×10^6	296.5	311.9	510.1
4.0×10^6	296.5	311.9	510.1

3.1. Experimental validation

The experimental configuration consists of five operating racks and two in-row CRAH units that use chilled water for extracting heat from racks. Figure 3 provides a schematic representation of the experimental DC facility. The widths of the cold and hot aisles are 0.14 m and 0.20 m, respectively, which are separated from one another by brushes to prevent energy and momentum transport across them. The numerical model is for a steady-state since the air temperature, and power measurements demonstrate negligible temporal variations. The experimental operating conditions for racks and cooling units are provided in Tables 7 and 8 respectively.

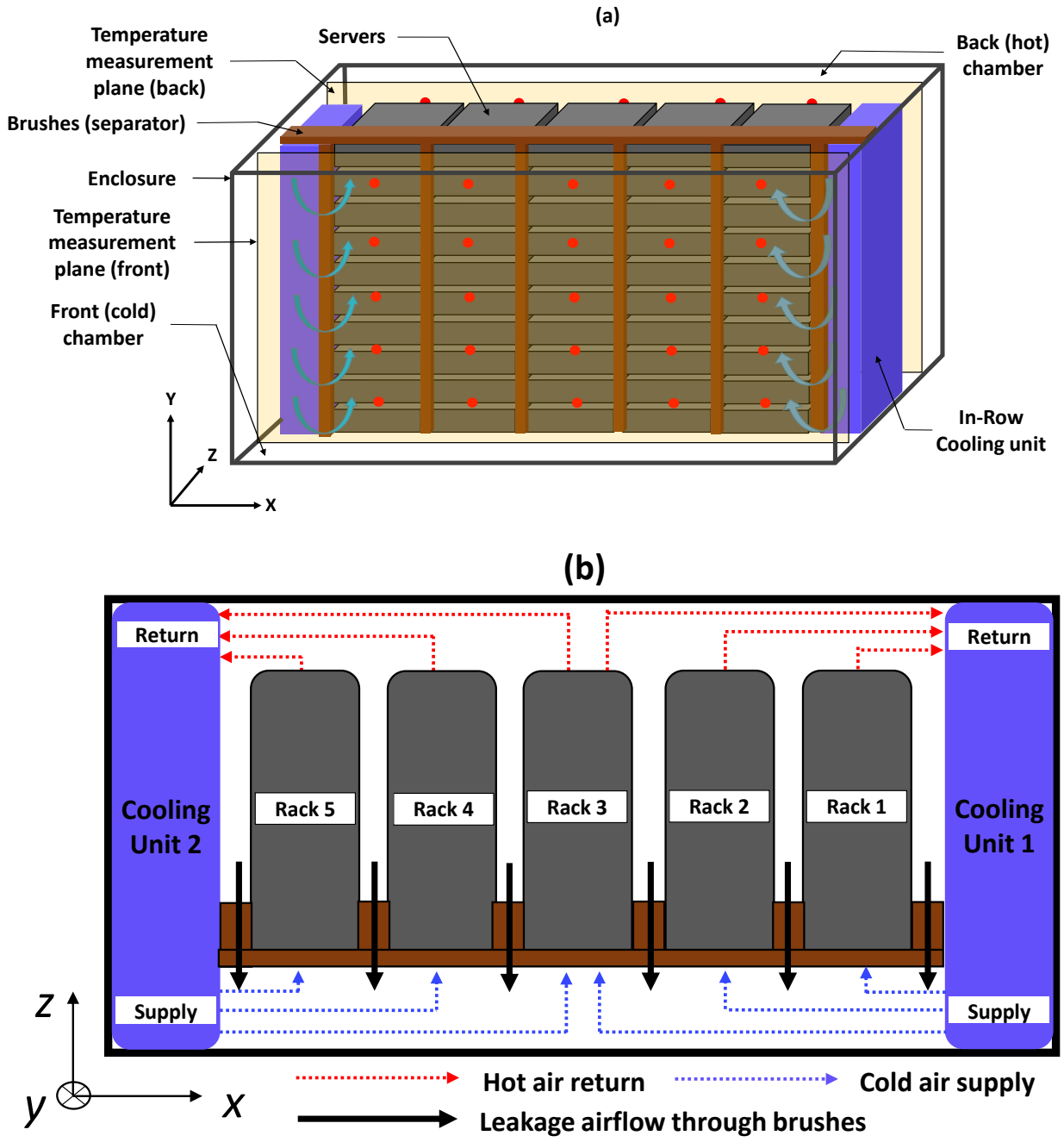

Figure 3: (a) Schematic representation of the experimental DC that has separated hot and cold chambers with 5 IT racks and 2 IRC units contained between them. In the aisle chamber, cold air exits the IRC and is drawn through the servers. Hot air exits the servers in the back aisle and is drawn into the IRC. Leakage airflow occurs through the brushes (or separators) across the aisles. Red dots indicate positions identifying the locations of temperature probes that are placed along the halfway plane of the width of the cold (Z = 0.06 m) and hot (Z = 1.22 m) aisles. (b) top cross-sectional view showing salient airflows. The direction of leakage airflow depends on the pressure difference across the front and back chambers.

Table 7: Rack operating conditions.

Rack	Volume flow rate of air ($m^3\ s^{-1}$)	It load (kW)
1	0.22	3.5
2	0.20	3.9
3	0.24	4.1
4	0.20	3.7
5	0.22	3.9

Table 8: Cooling unit operating conditions.

Case	Cooling unit	Volume flow rate of air ($m^3\ s^{-1}$)	Cooling unit set-point (°C)
1	Left Right	0.41 + 0.41	18
2	Left Right	0.51 + 0.51	

The heat transfer and fluid flow are simulated following the methodology in Section 4. The model assumes a complete conversion of the total IT load referred to in Table 7 into heat. The in-row cooling geometry shown in Figure 3 consists of a hot chamber, a cold chamber, and brushes that separates hot and cold chambers. Temperature measurements within the hot and cold chamber are performed with DS1820 temperature sensors that have an accuracy of ± 0.5 °C [44] and are connected to an Arduino Mega development board [45] that logs the data from 25 equidistant positions within each chamber. This provides the two-dimensional temperature distribution within each aisle along a plane halfway through the depth of aisles at Z = 0.06 m for cold aisle and Z = 1.22 m for hot aisle and represented by the red dots in Figure 3a. The percentage of error between CFD and experiments relative to the experimentally measured temperatures at each location is defined as follows,

$$\Delta = \frac{T_{CFD} - T_{EXP}}{T_{EXP}} \times 100\,. \tag{23}$$

Figure 4 shows contours of the distribution of the relative percentage error Δ between the CFD simulations and experiments for the scenarios presented in Table 8. For both cases in the cold aisle, eight locations show a 9% deviation from the experiments, while the remainder show Δ values of 5% or lower. For the hot aisle, there are only four positions for case 2 where Δ = 8%, whereas 11 locations show a deviation of 7.5% or lower. The primary reasons for differences between the experiments and CFD simulations are as follows. First, the power and network cable bundles placed in the hot aisle are not considered in the CFD simulations. This simplification is the primary source of error for temperature predictions in the hot aisle. Second, when the airflow into the server suction is lowered, the probability of hot air recirculating to the cold aisle increases, which diminishes the accuracy of predicted temperatures. However, a 10% temperature prediction deviation is considered acceptable for operational DCs [18, 25, 31].

Case	Cold Aisle	Hot Aisle
1	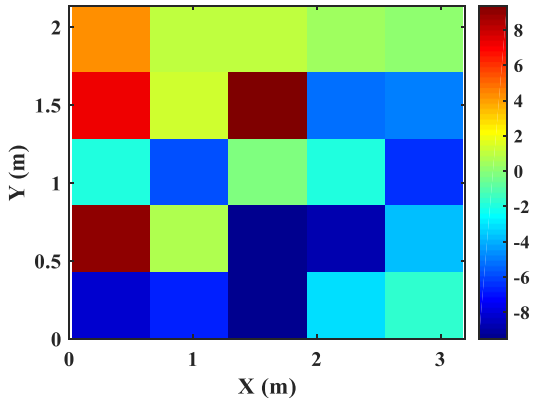	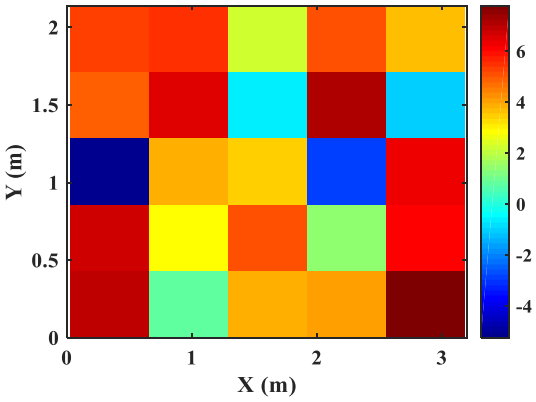
2	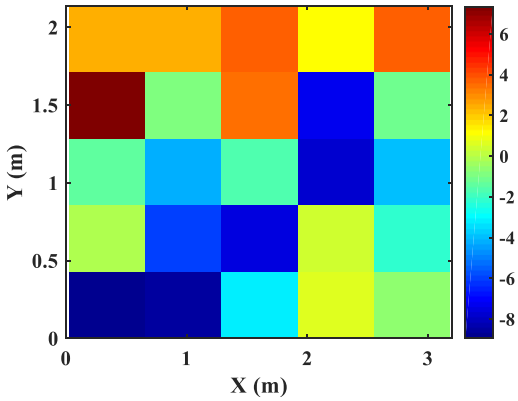	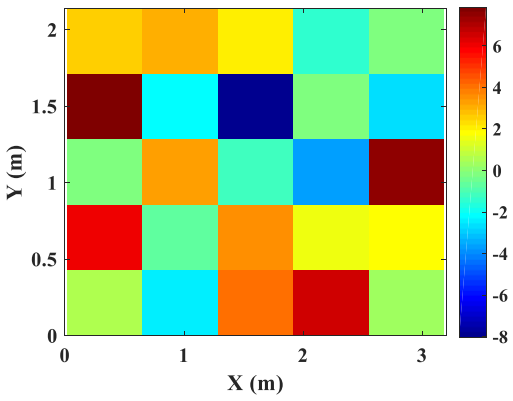

Figure 4: Distribution of Δ in the cold and hot aisles for two different validation cases presented in Table 8.

4. Results and discussion

4.1. Airside exergy loss

Airspace exergy destruction is caused by pressure drops, premature mixing of hot and cold airstreams, and turbulent fluctuations of energy and velocities. These effects are functions of (1) airflow path length, (2) cooling unit operating parameters, (3) number of cooling units, and (4) specific cooling architecture. The volume integral of the airspace exergy loss is determined for the scenarios and geometries depicted in Table 1.

Figure 5a shows the airspace exergy loss for different cooling architectures as a function of the CRAH unit airflow rate. The UFAD architecture has the highest exergy loss (up to 4 kW), which is caused by several factors [8]. They include the (1) uncontained geometry that leads to higher recirculation and bypass, which in turn increase the exergy loss due to heat transfer, (2) use of perforated tiles that produce a pressure drop in the underfloor plenum, increasing exergy destruction due to velocity gradients, and (3) higher flow rates that cause the air to bypass the perforated tile closest to the cooling unit, forming a flow void inside certain regions in the underfloor plenum, resulting in air ingress back from the room to the underfloor. The heat transfer exergy loss contributes ~67% of the total exergy destruction, while 33% of overall loss is due to the velocity gradients [18].

Compared with the UFAD architecture, the other geometries (OHAD, IRC, and RMCU) show up to 80% percent lower overall exergy loss in the airspace. This exergetic improvement is made possible by the corresponding localized air delivery schemes that reduce recirculation and bypass, and also eliminate pressure drop in the underfloor plenum [6, 18, 19].

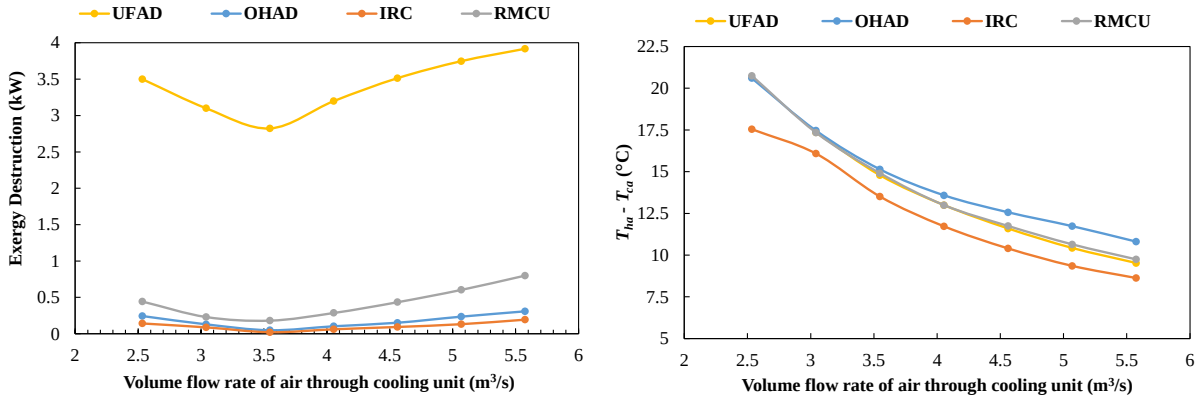

Figure 5: (a) airspace exergy loss, and (b) $T_{ha} - T_{ca}$ as a function of cooling unit airflow for different geometries.

For all geometries, increasing the airflow above a certain minimum (~3.5 $m^3\,s^{-1}$) increases the airspace exergy loss. This flowrate corresponding to the minimum exergy loss is the critical airflow for the DC, which occurs when the cooling unit airflow matches the total server air suction. Lower airflows lead to hot air recirculation occurs while higher values lead to server bypass. Hence, it is essential to identify the critical airflow when new servers are installed, or the idle servers are turned off [6, 23]. Figure 5b shows that increasing airflow monotonically decreases the difference between the supply and return temperatures ($T_{ha} - T_{ca}$). Since the airflow drawn by the servers is constant for all cases, the excess cold air is bypassed to the hot aisle through the porous brushes, lowering the mean air temperature in the hot aisle and the CRAH return.

Thus, several methods can be adopted to minimize airspace exergy loss, including, (1) reducing the airflow path length by switching to a localized cooling architecture, (2) implementing a contained air delivery scheme, (3) matching the total server suction with the cooling unit airflow using a predictive control algorithm, (4) decreasing the interaction between hot and cold aisles by using denser air-blocking brushes, and (5) hindering leakage across racks.

4.2. Heat exchanger exergy loss

Figure 6 presents the effect of cooling unit airflow variations on the CRAH exergy loss for different cooling architectures. The same fin-tube heat exchangers are used in the CRAH units for the UFAD and IRC architectures. In both cases, similar exergy loss variations are observed as the cooling unit airflow increases, where the loss first increases with increasing airflow and then decreases. However, the magnitude of exergy loss for the UFAD is 30% lower than for the IRC due to the higher effectiveness of the heat exchanger and the number of cooling units employed (one for UFAD and two for IRC). The OHAD architecture has nearly invariant exergy loss for all cases, but that for the RMCU progressively decreases by 33% as the volumetric flow rate is changed by 55%. We observe similar exergy destruction behaviors for UFAD and IRC heat exchangers and hence consider only one, the IRC, for additional comparison. However, the behaviors of RMCU and OHAD heat exchangers are very different, and both architectures must be considered. Thus, we examine the airside and waterside exergy destruction components of the IRC, RMCU, and OHAD architectures.

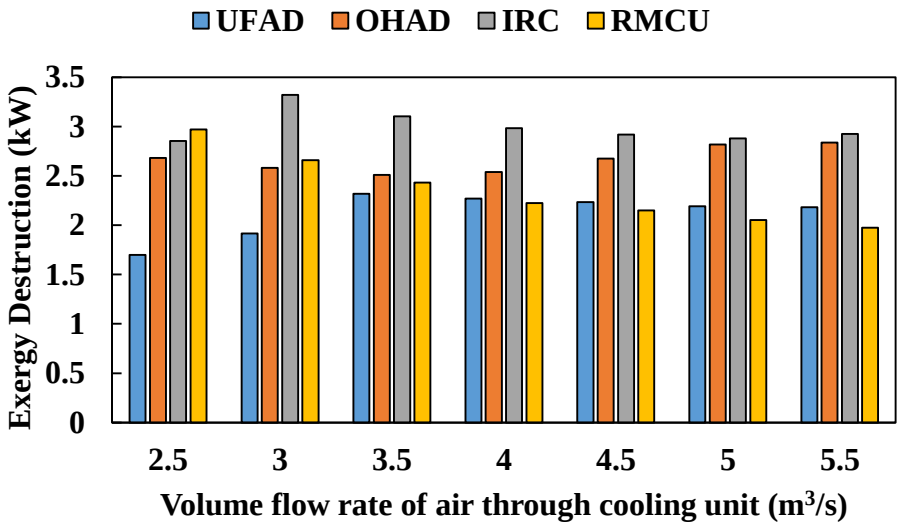

Figure 6: Heat exchanger exergy loss as a function of cooling unit airflow for different geometries.

The overall heat exchanger exergy loss is separated into (1) exergy gained by the waterside and (2) that lost by the air inside the heat exchanger. Figure 7a shows that exergy destruction for the OHAD heat exchanger has similar gradients on its waterside and airside, producing a nearly invariant total exergy loss with varying airflow. For the IRC architecture, the waterside exergy loss has a smaller gradient than on the airside (Figure 7b), but the overall exergy loss is again relatively invariant to changing airflow through the cooling unit. The RMCU heat exchanger is of plate-fin type, which has nearly invariant waterside exergy destruction with varying airflow (Figure 7c). However, due to the larger cold air bypass at elevated airflow, the return temperature to the heat exchanger decreases significantly (Figure 5b), decreasing $(T_{ha} - T_{ca})$ across it, resulting in a reduction in overall exergy loss.

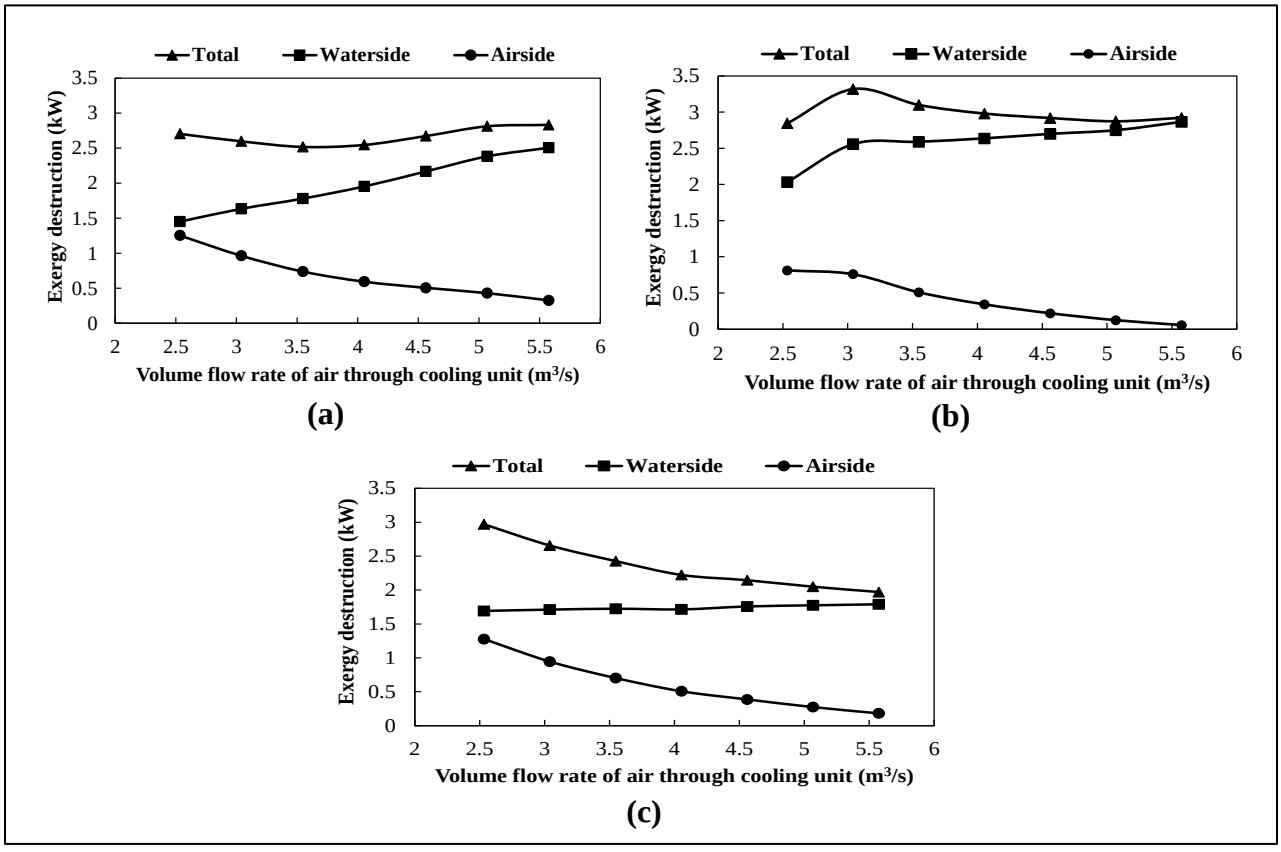

Figure 7: Airside and waterside components of the heat exchanger exergy loss for different geometries: (a) OHAD, (b) IRC, (c) RMCU

The exergetic efficiency for different heat exchangers [46],

$$\eta_{e,H} = \frac{\dot{\psi}_a}{\dot{\psi}_w} \times 100\,. \tag{24}$$

For the OHAD, IRC, RMCU, and UFAD architectures, the influence of cooling unit airflow on exergy efficiency is presented in Figure 8. When the airflow increases, the return temperature to the CRAH unit decreases due to the higher cold air bypass, which reduces the airside exergy destruction. This makes it more difficult to transfer heat from the airside to the waterside and reduces the exergetic performance of the heat exchanger. The fin-tube heat exchanger for the IRC has the lowest exergetic efficiency due to its lowest value of $T_{ha} - T_{ca}$ compared to the heat exchangers for RMCU and OHAD architectures (Figure 5b).

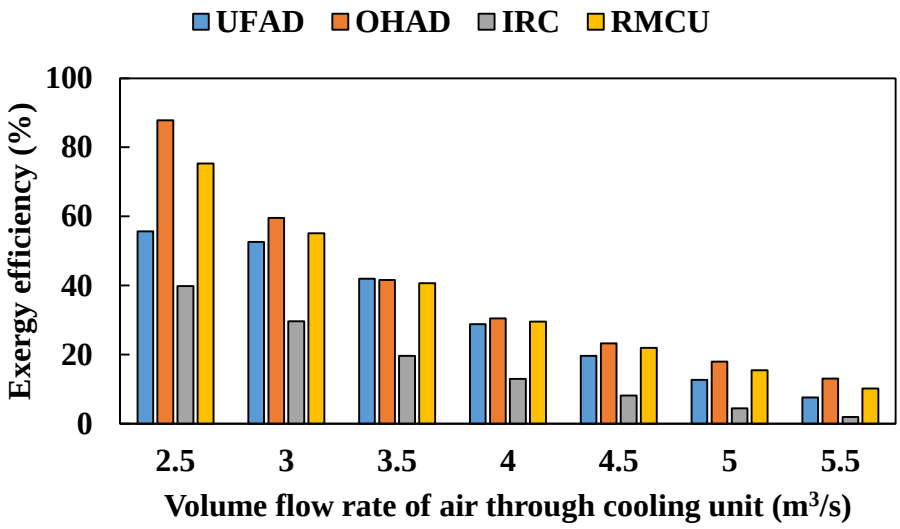

Figure 8: Influence of cooling unit airflow on the exergetic efficiencies of the heat exchangers used in the different architectures.

Although DCs typically employ additional cooling capacity in practice to support high network traffic loads, from an exergetic perspective, this increases exergy loss since the coolant

temperature can have values below T_0. Using a heat exchanger with greater effectiveness reduces irreversibility, decreasing the additional provisioning for cooling that is required [39].

4.3. Chiller exergy loss

Figure 9 presents the variation in chiller exergy loss for the different architectures as the airflow through the cooling unit is increased. By increasing the cold airflow within a DC for a constant cold air delivery set-point (see Table 1), the power consumption required for cooling also increases because this requires chilled water at lower temperatures. Hence, the temperature difference across the condenser side of the chiller increases since the chiller fans rotate at a constant speed and draw in air at a constant ambient temperature. This leads to an increment in the chiller exergy loss.

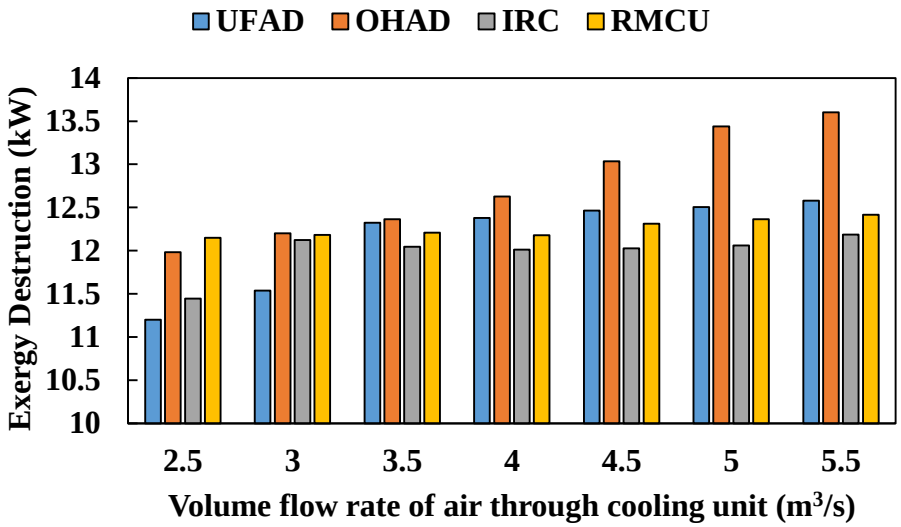

Figure 9: Influence of cooling unit airflow on the chiller exergy loss for different geometries.

The maximum exergy loss (~ 12.7 kW) inside the chiller occurs for the OHAD architecture when a 5.6 $m^3\ s^{-1}$ airflow is supplied through the cooling units. At higher flowrates (~ 4.1-5.6 $m^3\ s^{-1}$), the OHAD architecture again provides the highest chiller exergy destruction followed by the UFAD, IRC, and RMCU systems. The chiller exergy loss for the RMCU is nearly invariant with

changing airflow, while for the UFAD, OHAD, and IRC architectures, it increases due to the different characteristics of the heat exchangers that are used. The plate-fin heat exchanger used for the RMCU has a nearly invariant waterside exergy loss as the cooling unit airflow is increased (Figure 7c). Consequently the changes in chiller exergy loss are not significant with increasing airflow.

Designers should be careful while implementing algorithms for fan speed control in response to temperature increments in the cold aisle, since, in addition to fan power consumption the chiller exergy loss increases significantly as the fans inside CRAH are rotated at faster speeds. For proper control that minimizes exergy loss, it is therefore essential to simultaneously monitor CRAH fans and chillers.

The chiller exergy destruction is made dimensionless to compare the chiller exergy efficiencies for different cooling configurations as follows [47].

$$\eta_{e,c} = \left\{ 1 - \frac{\dot{\psi}_{d,c}}{\dot{W} + \dot{m}_w C_{pw} \left[\left(T_{hw} - T_0 \right) - T_0 \ln\left(\frac{T_{hw}}{T_0} \right) \right]} \right\} \times 100 \,. \tag{25}$$

Figure 10 shows the exergy efficiency of the chiller, which depends on the exergy loss and the exergy input to the chiller, as a function of the volumetric airflow through the cooling units of four different geometries. Except for the RMCU architecture, the exergy efficiency of a chiller improves with increasing airflow through a cooling unit. For the RMCU, the chiller exergy efficiency is independent of airflow. The IRC has the highest exergy chiller efficiency for the range of flowrates investigated. With increasing cooling unit airflow, the chiller heat load also increases and approaches its nominal design capacity. Near this heat load, the chiller works at higher COP and is, therefore, exergetically more efficient.

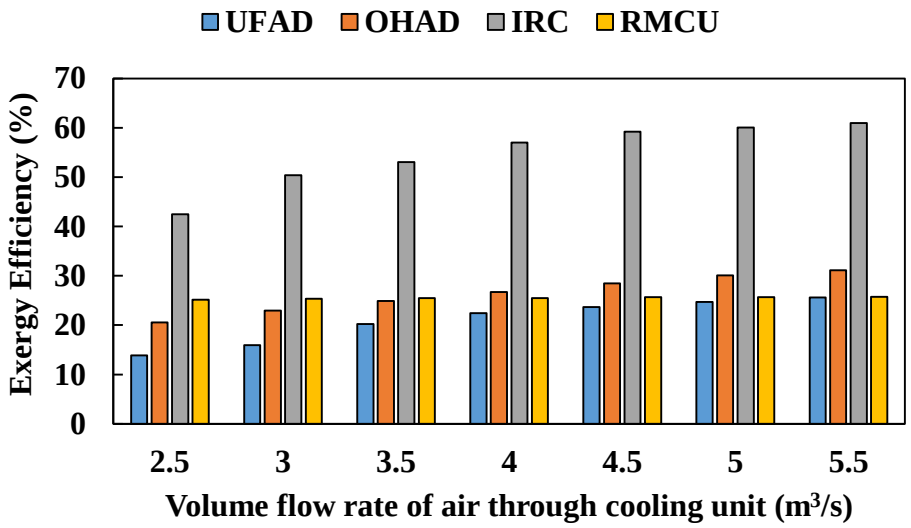

Figure 10: Influence of cooling unit airflow on the chiller exergy loss for different geometries.

4.4. Exergetic comparison of geometries under different scenarios

The exergy losses for the different components for the four architectures are compared in Figure 11 for three cooling unit flowrates, 3.04, 4.57 and 5.57 m^3s^{-1}, and a specified cold air supply set-point (see Table 1). The IRC and RMCU architectures outperform the room-based UFAD and OHAD legacy cooling by reducing hot air recirculation and cold air bypass. The rack exergy loss is the same for all cases due to the constant IT load imposed on the servers. The chiller exergy loss provides the highest contribution (~ 55% of the overall loss) to overall system inefficiency, followed by contributions from the rack and the heat exchanger.

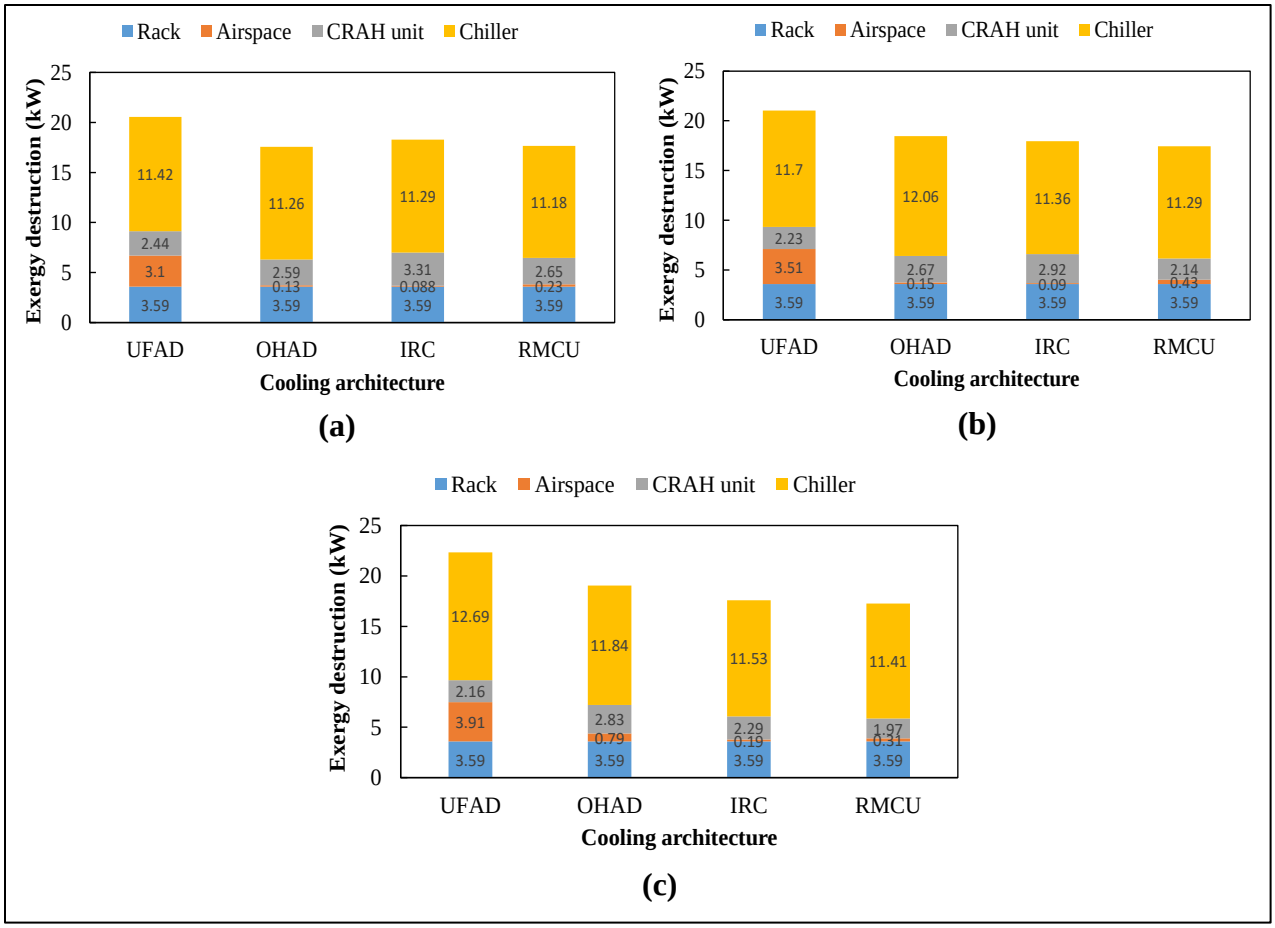

Figure 11: Contributions of different exergy loss components for the different cooling architectures with three different CRAH flowrates: (a) 3.04, (b) 4.57, and (c) 5.57 $m^3\,s^{-1}$.

For the UFAD architecture, the airspace exergy loss is significant (~ 3-4 kW) as compared to that of other schemes. This is predominantly due to the uncontained UFAD geometry, which leads to premature cold and hot air mixing. For the RMCU, the single rack cooling produces the minimum exergy loss due to locally effective air delivery for all air flowrates investigated, as shown in Figure 11. Changing from the UFAD to the OHAD, IRC or RMCU architectures can be represented by the parameter,

$$\Omega_g = \frac{\dot{\psi}_{UFAD} - \dot{\psi}_g}{\dot{\psi}_{UFAD}} \times 100\,. \tag{26}$$

Specifying the UFAD architecture as the base case, the overall exergy destruction for the OHAD, IRC, and RMCU architectures are compared in Table 9. For a 5.57 $m^3 s^{-1}$ airflow, the IRC and RMCU have 21.3% and 22.7% reductions in exergy loss, respectively, and the same trend holds for the 4.57 $m^3 s^{-1}$ flowrate. The OHAD architecture provides nearly constant exergetic savings (~12% to 14%) for the three flowrates. As the flowrates are reduced to 3.04 $m^3 s^{-1}$, the exergy loss is reduced to ~11-14%.

Table 9: Decrease in exergy loss for different architectures with respect to UFAD cooling.

Cooling unit airflow ($m^3 s^{-1}$)	Ω_{UFAD}	Ω_{OHAD}	Ω_{IRC}	Ω_{RMCU}
5.57	----	14.8	21.3	22.7
4.57	----	12.2	14.6	17.0
3.04	----	14.5	11.1	14.1

Figure 12 provides a schematic of the exergy behaviors along different components of an air-cooled DC, where arrow widths signify the relative magnitudes of exergy transfers. Ambient air entering the condenser corresponds to zero exergy since the condenser inlet air temperature is assumed to be equal to the dead state temperature.

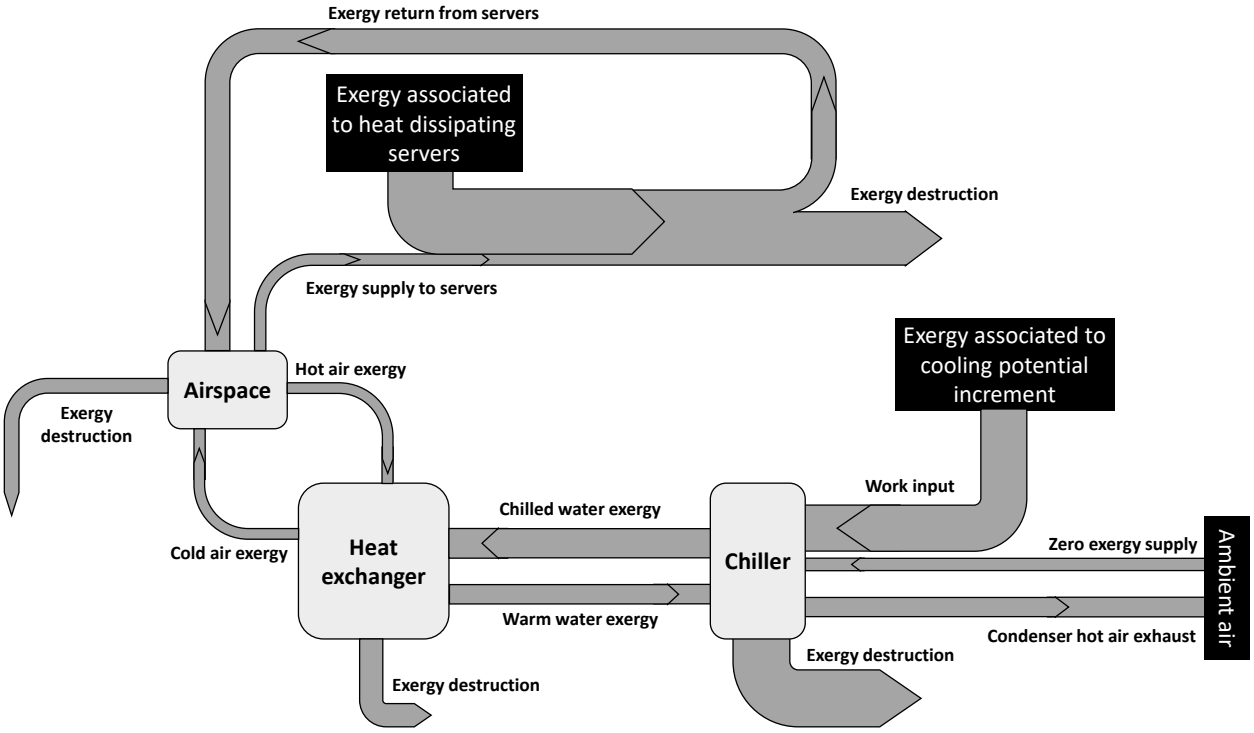

Figure 12: Schematic representation of exergy interactions in an air-cooled DC.

4.5. Dimensionless representation of exergy destruction

The overall exergy loss in the DC consists of four components, (1) in the racks due to heat dissipation, (2) in the airspace due to hot air recirculation and cold air bypass, (3) in the air-water heat exchanger, and (4) in the chiller. Because the cooling cycle exergy destruction is a function of total IT load $\dot{Q}_{IT}$ on a DC, the exergy loss is made dimensionless with respect to it. A higher IT load leads to a significant increment in the overall exergy destruction. The dimensionless exergy destruction is expressed using Eq. 27.

$$\eta = \frac{\dot{\psi}_{d,t}}{\dot{Q}_{IT}} = \frac{\dot{\psi}_{d,s} + \dot{\psi}_{d,a} + \dot{\psi}_{d,h} + \dot{\psi}_{d,c}}{\dot{Q}_{IT}}. \tag{27}$$

The second dimensionless parameter is the Peclet number, which is the ratio of advective to the diffusive heat transport in a DC, where

$$Pe = \frac{U_c L_c}{\alpha}. \tag{28}$$

Here, α denotes the thermal diffusivity of air. The characteristic CRAH velocity U_c represents the effect of flow, and a characteristic length L_c accounts for the influence of geometry, where the length is taken as the maximum distance travelled by air within a specific architecture. Both U_c and L_c are unique to an architecture and CRAH airflow. Thus, two central phenomena, (1) hot air recirculation and (2) cold air bypass, are addressed through *Pe*. Minimizing the two airspace inefficiencies associated with flow and geometry reduces the cascading exergy losses that occur in the CRAH and chiller. For the UFAD and IRC architectures, L_c is measured horizontally since air travels in that direction, whereas for OHAD and RMCU, it is taken along the vertical direction of air travel.

The third ratio is the dimensionless dead-state temperature ratio [18, 35, 39],

$$\zeta = \frac{T_0}{T_{ha} - T_{ca}}. \tag{29}$$

which compares the ambient dead state temperature T_0 to the difference in hot and cold aisle temperatures $\Delta T = T_{ha} - T_{ca}$. Flow recirculation and bypass indirectly influence ΔT by either increasing or decreasing the return air temperature to CRAH. A higher value increases hot air recirculation, producing a greater temperature nonuniformity in the airspace, which increases exergy loss. Further, raising the dead state temperature increases heat transfer irreversibility between the system and its surroundings, influencing the overall system irreversibility. Therefore, ζ is an essential parameter for comparing the enthalpy of the dead state the enthalpy rise across the hot and cold aisles in a DC.

Since the literature does not contain a specific dimensionless relation to express exergy loss as a function of the working parameters inside a DC, we correlate η with *Pe* and ζ. Figure 13

shows that the exergy loss per unit IT load η decreases with increasing ($Pe \times \zeta$), i.e., increasing either Pe or ζ reduces exergy destruction in a DC, for which the best fit obtained from Figure 13 is,

$$\eta = 0.3\left[Pe \times \zeta\right]^{-0.1}. \tag{30}$$

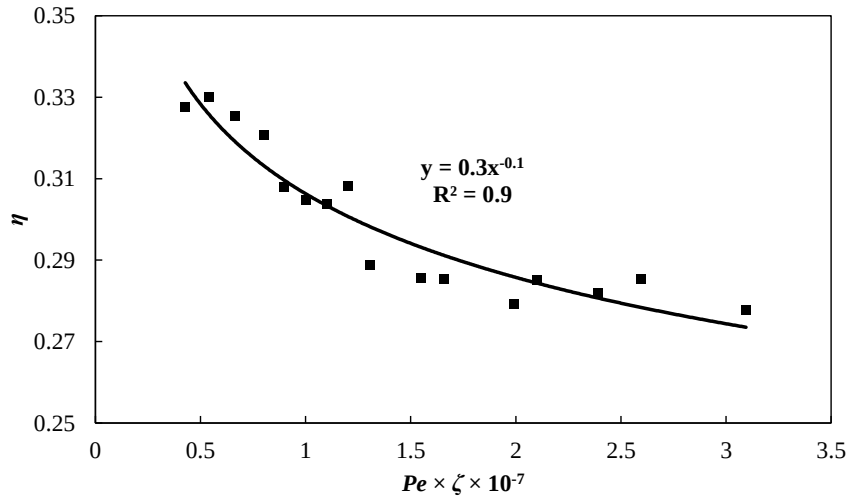

Figure 13: Dimensionless exergy loss η as a function of the dimensionless product ($Pe \times \zeta$).

It is impractical to increase the air velocity in a cooling unit beyond a specific value, and hence geometric modifications must be considered to minimize exergy loss, which can involve changing the cooling architecture. Solely from an exergetic perspective, operating a DC closer to ambient temperature decreases exergy destruction due to the reduction in exergy transfer to the ambient.

5. Conclusion

We provide an exergy destruction method to compare the performance of legacy DCs with emerging modular DCs. By employing the first and second laws of thermodynamics, system inefficiencies are represented as energy and exergy losses in a manner that can be used by DC

designers and operators. Simulated airflows inform the thermodynamic energy and exergy balances used to determine the exergy loss in the different components of an air-cooled DC. The effects of cooling geometry and operating parameters on the exergy loss in these components are investigated. Salient findings include:

1. The airspace exergy loss constitutes up to 20% of the total exergy loss for the UFAD architecture due to premature hot and cold air mixing and an underfloor pressure drop. For the other three architectures, the airspace contributes a much smaller ~5% of the total system exergy loss. Thereby, for DCs with UFAD architecture, the recirculation and bypass must be reduced by dynamically regulating airflows in real-time.
2. The chiller exergy loss has the highest contribution (~ 55 to 60%) towards the total exergy loss for all geometries and scenarios investigated. We have considered a vapor compression refrigeration chiller, which is widely used in DCs. This exergy loss can be minimized by recovering waste heat if thermally driven chillers, i.e., absorption chillers and adsorption chillers, are used instead.
3. Increasing the volumetric airflow of the cooling unit increases the chiller exergy loss progressively for all air delivery schemes. Hence, increasing the fan speed not only increases fan power consumption but also leads to higher chiller power consumption, which increases the exergy loss in the chiller. Thus, an exergy-aware coordinated control of CRAH fans and chillers should be implemented to minimize exergy and energy losses simultaneously.
4. For high cooling unit airflow, the exergy efficiency of the heat exchangers inside the CRAH decreases, whereas the chiller becomes exergetically efficient.

5. The UFAD configuration produces the highest exergy loss, while DCs with the modular RMCU has the lowest exergy destruction among four architecture. The RMCU has up to 23% lower overall exergy loss than the UFAD scheme.
6. The dimensionless exergy destruction η decreases monotonically with increasing ($Pe \times \zeta$).

Overall, we demonstrate the potential of second law analysis to improve air-cooled DC design, particularly to optimize its cooling and operation while reducing energy costs.

6. Acknowledgment

This research was supported by the Natural Sciences and Engineering Research Council (NSERC) of Canada through a collaborative research and development (CRD) project, "Optimizing Component Integration in Modular Data Centers". We thank colleagues from CINNOS Mission Critical Incorporated for helpful discussions.

7. Appendix

7.1. Process for exergy loss calculations

The RANS equations are used in combination with the widely used $k - \varepsilon$ model to represent turbulence, [6, 18-20, 31-33] and to resolve the characteristic airflow in DC. Governing equations for mass, momentum, energy, and turbulence, i.e., Eqs. (A1) through (A8) are numerically solved for each geometry and parametric test case using the commercial ANSYS Fluent 18.0 software. For a steady-state assumption adopted in this study, the continuity and RANS equations are [31],

$$\overline{\nabla} \cdot \overline{U} = 0 \tag{A1}$$

$$\overline{\nabla} \cdot (\overline{U}\overline{U}) = \frac{1}{\rho}\overline{\nabla} \cdot (\bar{\bar{\sigma}} - \rho\overline{U'}\overline{U'}) + \frac{1}{\rho}\bar{S} \tag{A2}$$

$$\bar{\bar{\sigma}} = -PI + \mu\{\overline{\nabla}(\overline{U}) + [\overline{\nabla}(\overline{U})]^T\} \quad \text{(A3)}$$

Where, $\bar{\bar{\sigma}}$ is the Newtonian stress tensor, μ is the dynamic viscosity of air, ρ is the density of air defined using an ideal gas equation of state, $\overline{U}$ and $\overline{U}'$ are the mean and turbulent velocity vectors, respectively, P is the pressure and I is the unit tensor. The momentum source term $\bar{S}$ of the RANS equation is only valid for the zones that contain the air blocking brushes in DC. The source term is calculated in FLUENT using a power-law approximation model as described using Eq. (1). The governing equations for the utilized standard $k-\varepsilon$ turbulence model are as follows,

$$\overline{\nabla} \cdot (k\overline{U}) = \frac{1}{\rho}\overline{\nabla} \cdot \left(\frac{\mu_t}{\rho_k}\overline{\nabla}(k)\right) + \frac{2\mu_t}{\rho} S_{ij} \cdot S_{ij} - \varepsilon \quad \text{(A4)}$$

$$\overline{\nabla} \cdot (\varepsilon\overline{U}) = \frac{1}{\rho}\overline{\nabla} \cdot \left(\frac{\mu_t}{\rho_\varepsilon}\overline{\nabla}(\varepsilon)\right) + C_{1\varepsilon}\frac{\varepsilon}{k\rho} 2\mu_t S_{ij} \cdot S_{ij} - C_{2\varepsilon}\frac{\varepsilon^2}{k} \quad \text{(A5)}$$

$$\mu_t = \rho C_\mu \frac{k^2}{\varepsilon} \quad \text{(A6)}$$

where, k is the turbulent kinetic energy, ε is the viscous dissipation rate, S_{ij} is the deformation tensor, and μ_t is the turbulent viscosity represented using Eq. A6. The model constants for the standard $k-\varepsilon$ model are, $C_\mu = 0.09, \rho_k = 1.0, \rho_\varepsilon = 1.3, C_{1\varepsilon} = 1.44$, and $C_{2\varepsilon} = 1.92$.

The energy equation utilizing $k-\varepsilon$ model can be written as,

$$\overline{\nabla} \cdot (T\overline{U}) = \overline{\nabla} \cdot \left(\left[\frac{\upsilon}{Pr} + \frac{\upsilon_t}{Pr_t}\right]\overline{\nabla}(T)\right), \quad \text{(A7)}$$

$$Pr = \frac{\upsilon}{\alpha} \text{ and } \alpha = \frac{\lambda}{\rho C_p}, \quad \text{(A8)}$$

where, Pr is the Prandtl number represented using Eq. A8, Pr_t is the turbulent Prandtl number, λ is the thermal conductivity of air, and C_p is the specific heat of air. For standard $k-\varepsilon$ model the value of Pr_t is 0.85.

The momentum and energy equations are discretized within the solution domain using a second-order upwind scheme, and first-order upwind is used to discretize the turbulent equations. The SIMPLE algorithm is used for pressure-velocity coupling. Exergy destruction within the airspace is calculated using Eqs. (5) – (9). Once the solver meets a specified convergence criterion when the residuals of all field variables reach 10^{-5}, the local exergy destruction within each control volume and subsequently its volume integral within the whole domain is computed using UDF in Fluent.

Once airspace convergence is obtained, the *ad hoc* heat exchanger model implemented in MATLAB™ (discussed in Section 3.4) determines the airside and waterside parameters required to calculate the exergy loss for the specific heat exchanger type (see Table 4). Further, the chiller power consumption and exergy destruction models (discussed in Section 3.5) are also used to determine the exergy loss in the chiller. A schematic representation of the numerical methodology is provided in Figure A1.

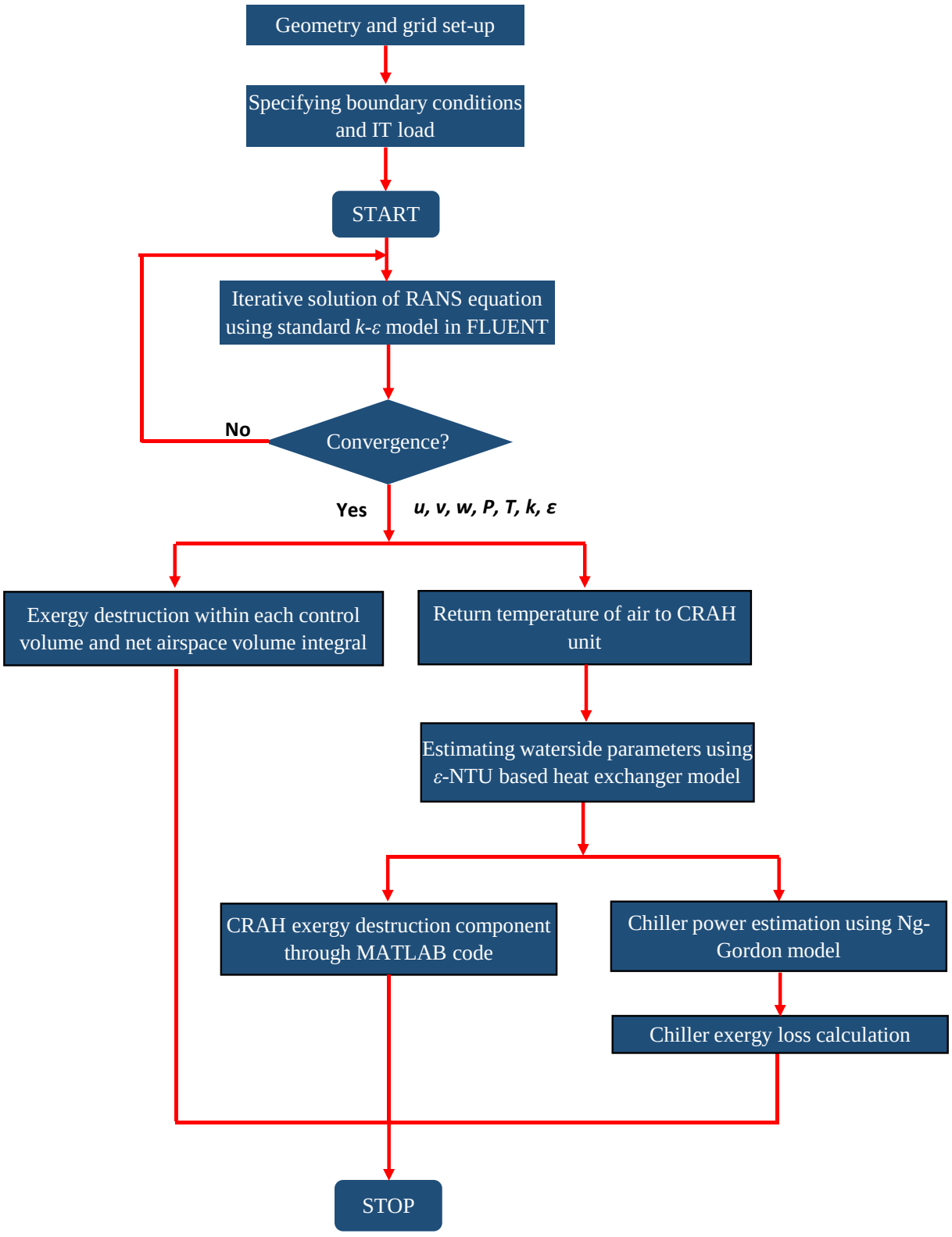

Figure A1: Schematic representation of the numerical procedure for computing exergy loss in the airspace, heat exchanger and chillers.

8. References

[1] N. Rasmussen, "Air distribution architecture options for mission critical facilities," *Elektron Journal-South African Institute of Electrical Engineers,* vol. 22, p. 68, 2005.

[2] A. Habibi Khalaj, T. Scherer, and S. K. Halgamuge, "Energy, environmental and economical saving potential of data centers with various economizers across Australia," *Applied Energy,* vol. 183, pp. 1528-1549, 2016/12/01/ 2016.

[3] K. Ebrahimi, G. F. Jones, and A. S. Fleischer, "Thermo-economic analysis of steady state waste heat recovery in data centers using absorption refrigeration," *Applied Energy,* vol. 139, pp. 384-397, 2015/02/01/ 2015.

[4] S. Zimmermann, M. K. Tiwari, I. Meijer, S. Paredes, B. Michel, and D. Poulikakos, "Hot water cooled electronics: Exergy analysis and waste heat reuse feasibility," *International Journal of Heat and Mass Transfer,* vol. 55, pp. 6391-6399, 2012/11/01/ 2012.

[5] S. Zimmermann, I. Meijer, M. K. Tiwari, S. Paredes, B. Michel, and D. Poulikakos, "Aquasar: A hot water cooled data center with direct energy reuse," *Energy,* vol. 43, pp. 237-245, 2012/07/01/ 2012.

[6] H. Moazamigoodarzi, P. J. Tsai, S. Pal, S. Ghosh, and I. K. Puri, "Influence of cooling architecture on data center power consumption," *Energy,* vol. 183, pp. 525-535, 2019/09/15/ 2019.

[7] K. Fouladi, J. Schaadt, and A. P. Wemhoff, "A novel approach to the data center hybrid cooling design with containment," *Numerical Heat Transfer, Part A: Applications,* vol. 71, pp. 477-487, 2017/03/04 2017.

[8] M. Xie, J. Wang, and J. Liu, "Evaluation metrics of thermal management in data centers based on exergy analysis," *Applied Thermal Engineering,* vol. 147, pp. 1083-1095, 2019/01/25/ 2019.

[9] K. Zhang, Y. Zhang, J. Liu, and X. Niu, "Recent advancements on thermal management and evaluation for data centers," *Applied Thermal Engineering,* vol. 142, pp. 215-231, 2018/09/01/ 2018.

[10] A. Capozzoli, G. Serale, L. Liuzzo, and M. Chinnici, "Thermal Metrics for Data Centers: A Critical Review," *Energy Procedia,* vol. 62, pp. 391-400, 2014/01/01/ 2014.

[11] A. H. Beitelmal and D. Fabris, "Servers and data centers energy performance metrics," *Energy and Buildings,* vol. 80, pp. 562-569, 2014/09/01/ 2014.

[12] A. J. Díaz, R. Cáceres, J. M. Cardemil, and L. Silva-Llanca, "Energy and exergy assessment in a perimeter cooled data center: The value of second law efficiency," *Applied Thermal Engineering,* vol. 124, pp. 820-830, 2017/09/01/ 2017.

[13] R. Khalid, A. P. Wemhoff, and Y. Joshi, "Energy and Exergy Analysis of Modular Data Centers," *IEEE Transactions on Components, Packaging and Manufacturing Technology,* vol. 7, pp. 1440-1452, 2017.

[14] X. Qian, Z. Li, and Z. Li, "Entransy and exergy analyses of airflow organization in data centers," *International Journal of Heat and Mass Transfer,* vol. 81, pp. 252-259, 2015/02/01/ 2015.

[15] A. J. Shah, V. P. Carey, C. E. Bash, and C. D. Patel, "Exergy Analysis of Data Center Thermal Management Systems," *Journal of Heat Transfer,* vol. 130, 2008.

[16] A. Bhalerao, K. Fouladi, L. Silva-Llanca, and A. P. Wemhoff, "Rapid prediction of exergy destruction in data centers due to airflow mixing," *Numerical Heat Transfer, Part A: Applications,* vol. 70, pp. 48-63, 2016/07/02 2016.

[17] K. Fouladi, A. P. Wemhoff, L. Silva-Llanca, K. Abbasi, and A. Ortega, "Optimization of data center cooling efficiency using reduced order flow modeling within a flow network modeling approach," *Applied Thermal Engineering*, vol. 124, pp. 929-939, 2017/09/01/ 2017.

[18] L. Silva-Llanca, A. Ortega, K. Fouladi, M. del Valle, and V. Sundaralingam, "Determining wasted energy in the airside of a perimeter-cooled data center via direct computation of the Exergy Destruction," *Applied Energy*, vol. 213, pp. 235-246, 2018/03/01/ 2018.

[19] L. Silva-Llanca, M. del Valle, A. Ortega, and A. J. Díaz, "Cooling Effectiveness of a Data Center Room under Overhead Airflow via Entropy Generation Assessment in Transient Scenarios," *Entropy*, vol. 21, p. 98, 2019.

[20] L. Silva-Llanca, M. del Valle, and A. Ortega, "The effectiveness of data center overhead cooling in steady and transient scenarios: comparison of downward flow to a cold aisle versus upward flow from a hot aisle," in *ASME 2015 International Technical Conference and Exhibition on Packaging and Integration of Electronic and Photonic Microsystems collocated with the ASME 2015 13th International Conference on Nanochannels, Microchannels, and Minichannels*, 2015.

[21] H. Moazamigoodarzi, S. Pal, S. Ghosh, and I. K. Puri, "Real-time temperature predictions in IT server enclosures," *International Journal of Heat and Mass Transfer*, vol. 127, pp. 890-900, 2018.

[22] S. Pal, H. Moazami-goodarzi, S. Ghosh, K. Thorn, and I. K. Puri, "Plate-fin heat exchanger suitable for rack-mountable cooling unit," ed: Google Patents, 2019.

[23] H. Moazamigoodarzi, S. Pal, D. Down, M. Esmalifalak, and I. K. Puri, "Performance of A Rack Mountable Cooling Unit in an IT Server Enclosure," *Thermal Science and Engineering Progress*, p. 100395, 2019.

[24] J. Priyadumkol and C. Kittichaikarn, "Application of the combined air-conditioning systems for energy conservation in data center," *Energy and Buildings*, vol. 68, pp. 580-586, 2014/01/01/ 2014.

[25] H. Moazamigoodarzi, R. Gupta, S. Pal, P. J. Tsai, S. Ghosh, and I. K. Puri, "Modeling temperature distribution and power consumption in IT server enclosures with row-based cooling architectures," *Applied Energy*, vol. 261, p. 114355, 2020.

[26] "Air-cooled liquid chillers, 10 to 60 Tons," in *Product Datasheet* vol. CG-PRC007-EN, TRANE, Ed., ed, 2004.

[27] "EC centrifugal fan, Model number: R3G250-RO40-A9," ebm-papst, Ed., ed, 2012.

[28] A. S. o. Heating, Refrigerating, A.-C. Engineers, and A. N. S. Institute, *Thermal environmental conditions for human occupancy* vol. 55: American Society of Heating, Refrigerating and Air-Conditioning Engineers, 2004.

[29] R. Steinbrecher and R. Schmidt, "Data center environments," *ASHRAE Journal*, vol. 53, pp. 42-49, 2011.

[30] W. M. Kays, A. L. London, and E. Eckert, "Compact heat exchangers," ed: American Society of Mechanical Engineers Digital Collection, 1960.

[31] A. Almoli, A. Thompson, N. Kapur, J. Summers, H. Thompson, and G. Hannah, "Computational fluid dynamic investigation of liquid rack cooling in data centres," *Applied energy*, vol. 89, pp. 150-155, 2012.

[32] V. K. Arghode and Y. Joshi, "Modeling strategies for air flow through perforated tiles in a data center," *IEEE Transactions on Components, Packaging and Manufacturing Technology*, vol. 3, pp. 800-810, 2013.

[33] V. K. Arghode, P. Kumar, Y. Joshi, T. Weiss, and G. Meyer, "Rack level modeling of air flow through perforated tile in a data center," *Journal of Electronic Packaging,* vol. 135, p. 030902, 2013.
[34] D. W. Demetriou, H. S. Erden, H. E. Khalifa, and R. R. Schmidt, "Development of an IT equipment lumped capacitance parameter database for transient data center simulations," in *Fourteenth Intersociety Conference on Thermal and Thermomechanical Phenomena in Electronic Systems (ITherm)*, 2014, pp. 1330-1337.
[35] A. Bejan, "Entropy generation minimization: The new thermodynamics of finite-size devices and finite-time processes," *Journal of Applied Physics,* vol. 79, pp. 1191-1218, 1996.
[36] F. Kock and H. Herwig, "Entropy production calculation for turbulent shear flows and their implementation in CFD codes," *International Journal of Heat and Fluid Flow,* vol. 26, pp. 672-680, 2005.
[37] F. Kock and H. Herwig, "Local entropy production in turbulent shear flows: a high-Reynolds number model with wall functions," *International journal of heat and mass transfer,* vol. 47, pp. 2205-2215, 2004.
[38] H. Herwig and F. Kock, "Direct and indirect methods of calculating entropy generation rates in turbulent convective heat transfer problems," *Heat and mass transfer,* vol. 43, pp. 207-215, 2007.
[39] A. Bejan, *Entropy generation minimization: the method of thermodynamic optimization of finite-size systems and finite-time processes*: CRC press, 2013.
[40] "CRAC Precision climate control units for data centers, Model number: 3300.387," in *Product Datasheet*, RITTAL, Ed., ed, 2014.
[41] "TopTherm LCP rack/inline CW, Model Number: 3311.130," in *Product datasheet* vol. 530, RITTAL, Ed., ed, 2015.
[42] J. Gordon and K. Ng, "Cool Thermodynamics, Cambridge Int," in *Science*, ed, 2000.
[43] E. Cruz and Y. Joshi, "Inviscid and viscous numerical models compared to experimental data in a small data center test cell," *Journal of Electronic Packaging,* vol. 135, p. 030904, 2013.
[44] R. Gupta, C. Das, A. Datta, and R. Ganguly, "Background Oriented Schlieren (BOS) imaging of condensation from humid air on wettability-engineered surfaces," *Experimental Thermal and Fluid Science,* vol. 109, p. 109859, 2019.
[45] R. Gupta, C. Das, A. Roy, R. Ganguly, and A. Datta, "Arduino based temperature and humidity control for condensation on wettability engineered surfaces," in *2018 Emerging Trends in Electronic Devices and Computational Techniques (EDCT)*, 2018, pp. 1-6.
[46] T. K. Ray, A. Datta, A. Gupta, and R. Ganguly, "Exergy-based performance analysis for proper O&M decisions in a steam power plant," *Energy Conversion and Management,* vol. 51, pp. 1333-1344, 2010/06/01/ 2010.
[47] J. U. Ahamed, R. Saidur, and H. H. Masjuki, "A review on exergy analysis of vapor compression refrigeration system," *Renewable and Sustainable Energy Reviews,* vol. 15, pp. 1593-1600, 2011.